Fuel 358 (2024) 130166

Contents lists available at ScienceDirect

Fuel

journal homepage: www.elsevier.com/locate/fuel

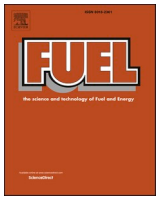

Full Length Article

Dry reforming of methane over sub-stoichiometric $NiAl_2O_4$-mediated Ni/Al_2O_3 catalysts

Andoni Choya [a], Beatriz de Rivas [a], María Luisa No [b], Jose Ignacio Gutiérrez-Ortiz [a], Rubén López-Fonseca [a,*]

[a] Chemical Technologies for Environmental Sustainability Group, Department of Chemical Engineering, Faculty of Science and Technology, University of The Basque Country UPV/EHU, Barrio Sarriena s/n, Leioa, Bizkaia E-48940, Spain
[b] Department of Physics, Faculty of Science and Technology, University of The Basque Country UPV/EHU, Barrio Sarriena s/n, Leioa, Bizkaia E-48940, Spain

ARTICLE INFO

Keywords:
Dry reforming
Methane
Nickel
Aluminate
Dispersion
Substoichiometric precursor

ABSTRACT

A series of Ni/Al_2O_3 catalysts were prepared from substoichiometric $NiAl_2O_4$ precursors (Ni/Al molar ratio between 0.5 and 0.05) were examined for the dry reforming of methane. The calcined spinel precursors and the corresponding reduced catalysts were characterised by N_2 physisorption, X-ray fluorescence, X-ray diffraction, Raman spectroscopy, electronic microscopy coupled to elemental mapping, X-ray photoelectron spectroscopy and temperature-programmed techniques. Compared with the stoichiometric counterpart, nickel species present in Ni-deficient precursors were mostly in the form of a spinelic phase. After high-temperature reduction, narrow particle size distributions centred at 10 nm were obtained. The largest available nickel surface area (18 $m^2\,g^{-1}$) was exhibited by the catalyst derived from the precursor with a Ni/Al of 0.15. The $NiAl_2O_4$-mediated catalysts, especially those with Ni/Al molar ratio in the 0.15–0.25 range, exhibited a notable performance at 90,000 h^{-1} and 650 °C. The optimal catalyst (14%wt.%Ni), with 93%CH_4 and 80%CO_2 conversions, was also able to operate for 200 h despite the significant formation of carbonaceous nanotubes (around $1 g_C\, g_{CAT}^{-1}$) and were examined.

1. Introduction

Climate change and the increasingly scarce reserves of fossil fuels are driving governments and other entities towards the use of low-carbon energies and the development of technologies that allow for maintaining the economy growth without damaging the environment. In this sense, the implementation of CO_2 capture and storage technologies is a key element for sustainable development, since these processes reduce the CO_2 emissions of numerous sources such as thermal energy plants, steel works, cement works or wastewater treatment plants, among others [1,2]. Moreover, the captured CO_2 can be utilised in several applications, from food processing and packaging to fire suppression or as a raw material in chemical synthesis. More importantly, captured CO_2 can be used to produce high-value syngas, which, in turn, can be further employed in the production of liquid fuels or highly pure hydrogen [3,4].

The most common industrial route for the production of syngas is steam reforming of natural gas, from which grey hydrogen can be obtained [5,6]. However, steam reforming presents several drawbacks, with the most important one being its high-energy requirements [7]. Moreover, steam reforming generates significant amounts of CO_2, which can be critical if the process is focused on hydrogen production, since the CO generated in the reaction must be converted into CO_2 in a subsequent water–gas shift step [8]. This makes the implementation of an additional CO_2 capture system necessary.

A possible alternative to this strategy is the dry reforming of methane (DRM), which is the reaction where methane is partially oxidised with CO_2. This process presents important environmental benefits since it utilises two greenhouse gases to produce syngas, effectively consuming CO_2 instead of generating it [9]. Furthermore, its requirements in terms

Abbreviations: BET, Brunauer-Emmett-Teller surface area; BJH, Barrett-Joyner-Halenda method; DRM, Dry Reforming of Methane; EDS, Energy-Dispersive X-ray Spectroscopy; FFT, Fast Fourier Transform; H_2-TPR, Temperature-Programmed Reduction with Hydrogen; HAADF, High-Angle Annular Dark Field imaging; HRTEM, High-Resolution Transmission Electron Microscopy; ICDD, International Centre for Diffraction Data; IUPAC, International Union of Pure and Applied Chemistry; MS, Mass Spectrometry; RWGS, Reverse Water Gas Shift; STEM, Scanning Transmission Electron Microscopy; TEM, Transmission Electron Microscopy; TGA, Thermogravimetric Analysis; WDXRF, Wavelength Dispersive X-ray Fluorescence; XPS, X-ray photoelectron spectroscopy; XRD, X-Ray Diffraction.

* Corresponding author.
E-mail address: ruben.lopez@ehu.eus (R. López-Fonseca).

https://doi.org/10.1016/j.fuel.2023.130166
Received 26 July 2023; Received in revised form 28 September 2023; Accepted 22 October 2023
Available online 31 October 2023

Table 1
Physico-chemical properties of the $NiAl_2O_4$ precursors.

Sample	Nominal Ni/Al molar ratio	Actual Ni/Al molar ratio	Ni loading, %wt.	S_{BET}, m^2/g^{-1}	V_{pore}, $cm^3\ g^{-1}$	$NiAl_2O_4$ crystallite size, nm	Cell parameter, Å	NiO crystallite size, nm
NiAl(5)	0.05	0.05	5	122	0.30	4	7.9294	–
NiAl(10)	0.10	0.11	10	112	0.28	6	7.9449	–
NiAl(14)	0.15	0.16	14	105	0.28	7	7.9634	–
NiAl(18)	0.20	0.22	18	99	0.27	8	7.9794	–
NiAl(21)	0.25	0.27	21	93	0.26	9	7.9994	9
NiAl(24)	0.30	0.33	24	90	0.23	9	8.0052	8
NiAl(29)	0.40	0.42	29	75	0.20	9	8.0116	7
NiAl(33)	0.50	0.54	33	71	0.20	10	8.0115	7

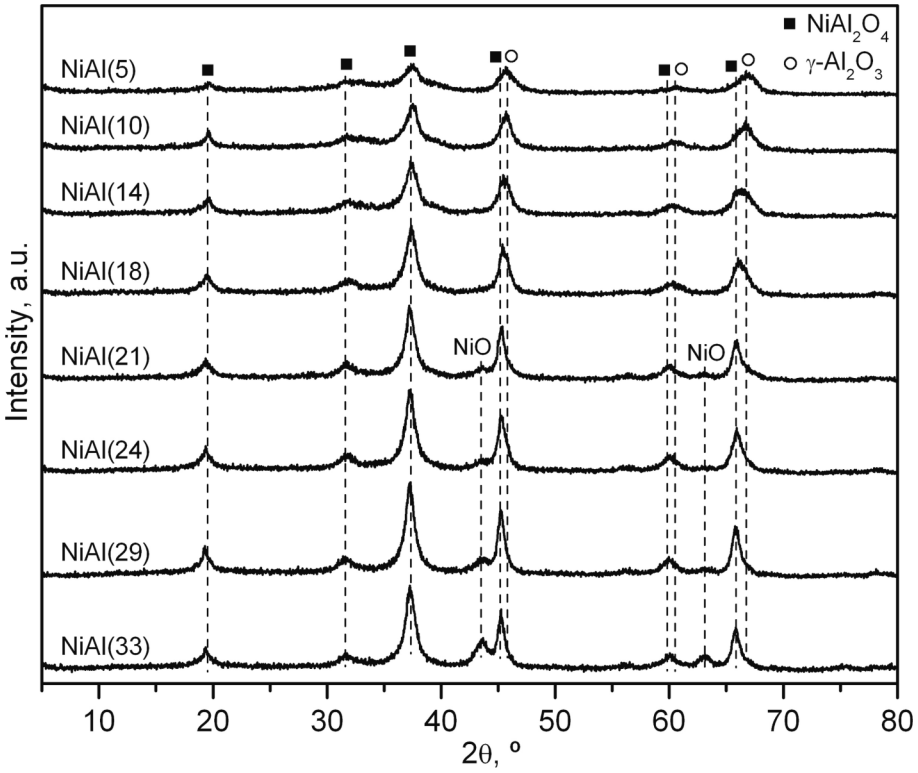

Fig. 1. X-Ray diffractograms of the $NiAl_2O_4$ precursors.

of purity of the feedstock are notably lower with respect to steam reforming, thus being able to profitably process low-value streams such as landfill biogas, anaerobic digestion biogas or mine gas [10,11]. The main shortcoming of this reaction is its significant endothermicity, which makes necessary the presence of an efficient catalyst working at moderate temperatures (650–750 °C) without being severely affected by deactivation upon sintering and coking [12]. In this sense, since two sources of carbon are present in the feedstream, the effect of coking on the catalyst is inherently more intense [13].

It is widely accepted that four elementary steps are involved in DRM [14,15]: (i) dissociative adsorption of methane, (ii) dissociative adsorption of CO_2, (iii) formation of surface hydroxyl groups and water, and (iv) oxidation of CH_x species, along with the formation and desorption of CO and H_2. The first step is the rate-determining step, and involves the generation of a trigonal pyramidal structure by electron interactions between the adsorbed methane molecule and the active metal particle. However, CO_2 dissociative adsorption on the metal-support interface in various possible coordination geometries is generally considered as a fast step. Current understanding of the last two steps is still rather limited. Hydroxyl groups are expected to form when hydrogen migrates from the active metal surface to the support and reacts with the oxygen species on the support. The oxidation of CH_x ($0 \leq x \leq 3$) by surface oxygen leads to the formation of CH_xO or CO on the catalyst surface.

Typically, catalysts based on highly dispersed metallic nickel have been proven the most attractive systems [16,17], frequently surpassing noble metal catalysts. Traditionally, these catalysts have been prepared from the reduction at moderate temperatures of NiO supported over porous media such as gamma alumina [18,19]. However, this route tends to produce catalysts with large Ni crystals (40–80 nm), which are more prone to deactivation by coking and sintering [20]. In addition, Ni can easily react with γ-Al_2O_3 to form nickel aluminate at relatively mild temperatures, thereby irreversibly fixing a significant amount of Ni^{2+} cations and concomitantly lowering the content of the available active phase [21]. An alternative approach might just be to turn what would be an undesirable effect into a virtue with a high potential for catalytic applications. Thus, the proposal in this case would consist of forcing the formation by high-temperature calcination (above 800 °C) of a highly crystalline $NiAl_2O_4$ bulk phase in which the added nickel will be properly integrated into the structure of this spinel [22]. After an appropriate reduction treatment, a Ni/Al_2O_3 catalyst characterised by relatively small crystallite sizes (10–30 nm) and high nickel dispersions would be

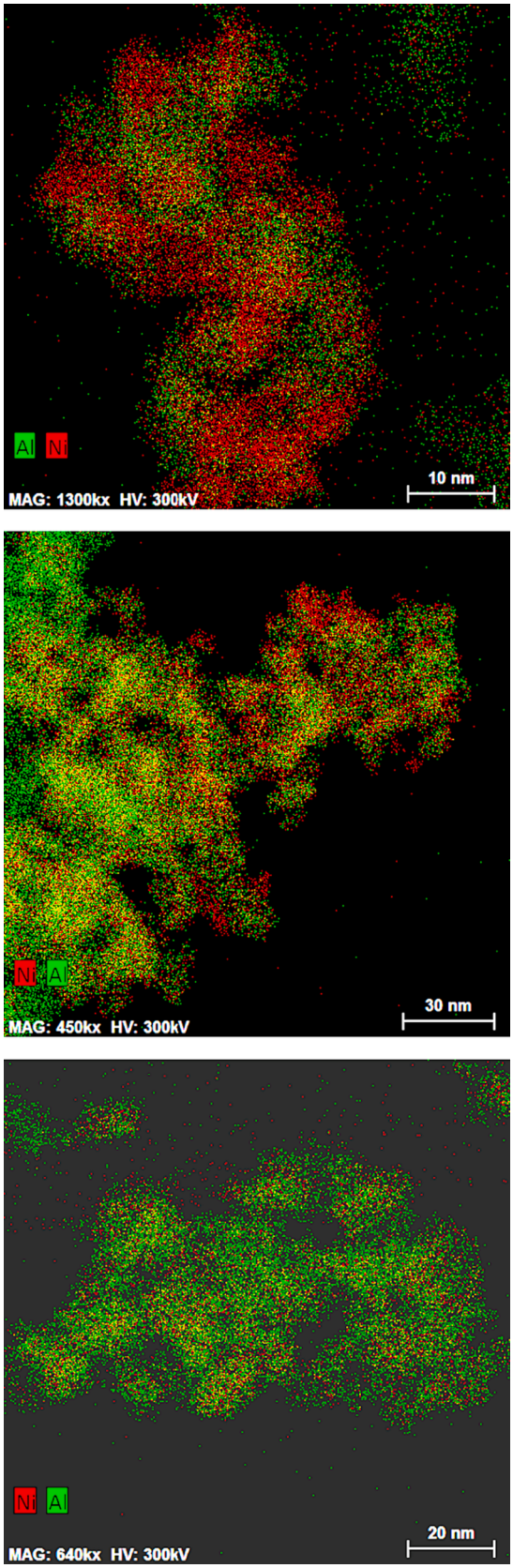

Fig. 2. STEM/EDS elemental maps of the stoichiometric (NiAl(33) (figure at the top), sub stoichiometric (NiAl(21) (figure in the middle) and sub-stoichiometric (NiAl(14) (figure at the bottom) $NiAl_2O_4$ precursors.

obtained. These physico-chemical features are expected to give higher activities at moderate temperatures and a remarkable resistance to coking and uncontrollable growth of the metal crystallites [23].

Several examples of this approach can be found in the literature. For instance, Boukha et al. [24] found a $NiAl_2O_4$-derived catalyst prepared by coprecipitation highly active for partial oxidation, steam reforming and oxidative steam reforming of methane. On the other hand, Fang et al. [25] also found $NiAl_2O_4$-based catalysts active for the steam reforming of propane. Similarly, this type of catalysts has been proven active for the steam reforming of various compounds such as ethanol [26], toluene [27], isooctane [28] or bio-oil [29]. Morales-Marín et al. [30] even found them active for the reforming of glycerol in aqueous phase. Regarding dry reforming of methane, various research works have studied the benefits of employing stoichiometric $NiAl_2O_4$ as precursor for producing Ni/Al_2O_3 catalysts, with all of them finding that this approach results in smaller Ni crystallite sizes characterised by a high intrinsic activity [31,32].

However, the use of the stoichiometric nickel aluminate as catalytic precursor is also not exempt from disadvantages. Since the Ni loading of nickel aluminate is near 33% in weight, after reduction the resulting catalyst can present a metallic nickel loading of up to 37%wt.Ni, which is notably high for a supported catalyst. Under these conditions, the formed nickel crystallites will still be large and poorly dispersed. The use of Ni/Al_2O_3 catalysts with low Ni loadings (<15%wt.) has been also explored in the literature. Numerous studies reported that those catalysts can outperform those with higher contents in terms of both activity and stability due to their higher metallic dispersions [33,34].

Interestingly, the combination of the two aforementioned approaches, that is, the use of $NiAl_2O_4$ spinels with a sub-stoichiometric Ni/Al molar ratio (lower than 0.5) can be a smart alternative to overcome these issues. By preparing a precursor with a lower nickel loading, the resulting catalyst is expected to exhibit a smaller crystal size and higher dispersion. Such systems have been already successfully applied for the steam reforming reaction [35], but are yet to be extensively investigated for the dry reforming of methane. For these reasons, in this work we propose the optimisation of the Ni/Al molar ratio of $NiAl_2O_4$-like precursor between 0.5 and 0.05, with the aim of producing highly efficient supported Ni/Al_2O_3 catalysts with varying Ni content (5–33% wt.) for the DRM reaction, conducted at 650 °C and 90,000 h^{-1} for a prolonged reaction time interval (200 h). Comparing with most studies on dry reforming these selected operating conditions are rather demanding from a catalytic point of view as coke formation is thermodynamically favoured at low temperatures, the residence time is short (<0.05 s) and the corresponding weight hourly space velocity is as high as 72,000 mL CH_4 g^{-1} h^{-1}.

2. Experimental

2.1. Synthesis of the Ni/Al_2O_3 catalysts based on substoichiometric nickel aluminates

The synthesis of the $NiAl_2O_4$-like precursors was carried out by co-precipitation of solutions of nickel (II) nitrate hexahydrate ($Ni(NO_3)_2{\cdot}6H_2O$) and aluminium (III) nitrate nonahydrate ($Al(NO_3)_3{\cdot}9H_2O$) with a solution of sodium carbonate (Na_2CO_3) 1.2 M. The concentration of the solutions was adjusted to prepare eight precursors with varying Ni/Al molar ratio between 0.05 and 0.5, namely 0.05, 0.1, 0.15, 0.2, 0.25, 0.3, 0.4 and 0.5. The sodium carbonate solution was added dropwise at constant temperature (80 °C) until the pH reached 9. After filtration and drying (110 °C), the formed precipitates were calcined at 850 °C for 4 h to obtain the thermally stabilised oxides [30]. The aluminate precursors were labelled as NiAl(x), where x denoted the Ni weight percentage. To obtain the catalytically active Ni/Al_2O_3 samples, the precursors were subjected to an in-situ reduction step at 850 °C for 2 h with a 5%H_2/N_2 mixture.

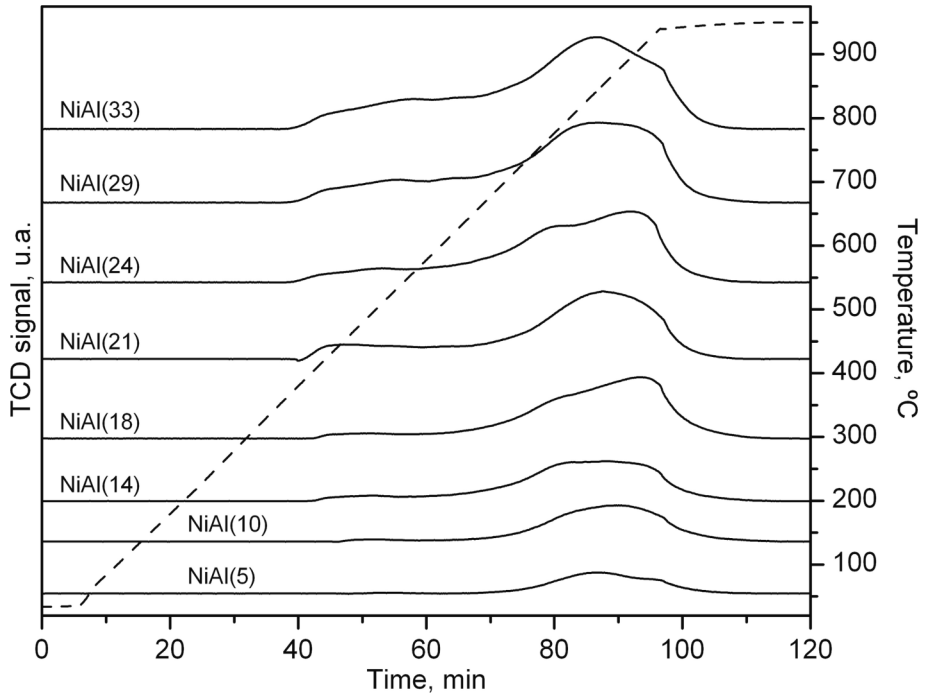

Fig. 3. H_2-TPR profiles of the $NiAl_2O_4$ precursors.

Table 2
H_2 uptake of the $NiAl_2O_4$ precursors from the H_2-TPR analysis.

Sample	Low-temperature (50–650 °C) H_2 uptake, mmol g^{-1}	High-temperature (650–950 °C) H_2 uptake, mmol g^{-1}	$NiAl_2O_4$ fraction, %
NiAl(5)	0.02	0.92	98
NiAl (10)	0.11	1.49	93
NiAl (14)	0.25	2.12	90
NiAl (18)	0.37	2.59	88
NiAl (21)	0.66	2.87	81
NiAl (24)	0.89	3.10	78
NiAl (29)	1.34	3.62	73
NiAl (33)	1.67	3.90	70

Table 3
Physico-chemical properties of the reduced Ni/Al_2O_3 catalysts.

Sample	S_{BET}, m^2/g^{-1}	V_{pore}, cm^3 g^{-1}	Ni crystallite size (XRD), nm	Ni crystallite size (STEM/HAADF), nm
NiAl(5)	96	0.22	8	12
NiAl (10)	88	0.22	10	15
NiAl (14)	85	0.21	10	15
NiAl (18)	78	0.20	11	17
NiAl (21)	70	0.20	12	19
NiAl (24)	68	0.18	12	19
NiAl (29)	57	0.16	12	25
NiAl (33)	54	0.15	15	29

2.2. Characterisation techniques

The textural properties of the calcined oxide precursors and the reduced catalysts, namely the specific surface area, the pore volume and the pore size distributions, were determined by N_2 adsorption/desorption in a Micromeritics Tristar II apparatus at 77 K. Prior to the analysis, each sample was subjected to degassing at 300 °C for 10 h in a Micromeritics SmartPrep degasser. The specific surface area of the samples was calculated from the adsorption isotherm using the BET (Brunauer-Emmett-Teller) method, while the pore volume and pore size distributions were determined from the desorption branch using the BJH (Barrett-Joyner-Halenda) method. The elemental composition of the NiAl(x) samples was determined by Wavelength Dispersive X-Ray Fluorescence (WDXRF) in a PANalytical AXIOS sequential spectrometer equipped with a Rh tube and three different detectors. The analysis was made over boron-glass pearls prepared by fusion, in an induction micro-furnace, of the samples with the flux agent Spectromelt A12 in a 20:1 proportion.

X-Ray diffraction (XRD) experiments were carried out on a X'PERT-PRO X-ray diffractometer equipped with a Cu K_α ($\lambda = 1.5406$ Å) X-Ray source that was operated at 40 kV and 40 mA and a Ni filter. The diffractograms were taken between the 2θ positions of 5 and 80° with a step size of 0.026°. The analysis by Raman spectroscopy of the catalysts was carried out by using a Renishaw InVia Raman spectrometer, coupled to a Leica DMLM microscope. The analysis was performed in the spectral window of 1100–1800 cm^{-1} using 10% of the maximum power of a Modu-Laser ion-argon laser with an excitation wavelength of 514 nm. The spatial resolution was 2 μm and for each spectrum 20 s were employed and 5 scans were accumulated.

The samples for transmission electron microscopy were dispersed in absolute ethanol ultrasonically, and the solutions were then dropped on copper grids coated with lacey carbon film. The characterisation of the samples by transmission and scanning-transmission electron microscopy (TEM and STEM) was carried out on a FEI Titan Cubed G2 60–300 kV, operating at 300 kV, with a gun monochromator, a Cs-objective aberration corrector (Ceos) and a super-X detector, with four X-ray silicon drift detectors. High-angle annular dark field (HAADF) images, as well

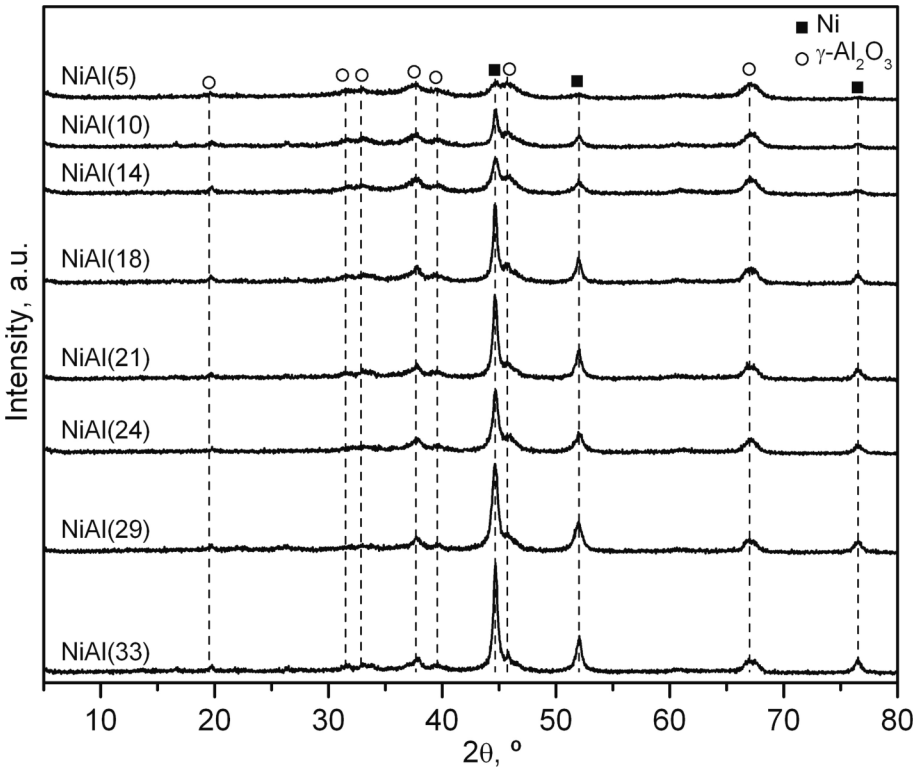

Fig. 4. X-Ray diffractograms of the reduced $NiAl_2O_4$ precursors.

as qualitative and quantitative energy dispersive X-ray spectroscopy (EDS) mapping, were obtained in STEM mode. For the EDS maps, beam currents between 0.15 and 0.21 nA, 900 s per map with scans of 6 s, and a drift correction system were used. The quantitative analysis was performed considering a thickness of 10 nm and the Cliff-Lorimer factors. High-resolution images were obtained in TEM mode (HRTEM) and the fast Fourier transform (FFT) of the images was also applied.

The reducibility of the sub-stoichiometric Ni/Al precursors was investigated on a Micromeritics Autochem 2920 apparatus by temperature-programmed reduction with hydrogen (H_2-TPR). The experiments were carried out using a 5%H_2/Ar mixture as the reducing agent from ambient temperature to 950 °C with a heating rate of 10 °C min^{-1}. This temperature was maintained for 30 min. The samples were additionally characterised by X-Ray photoelectron spectroscopy (XPS). Spectra were collected with a Kratos AXIS Supra spectrometer (225 W Al Kα radiation source) with a pass energy of 20 eV. The conductivity of the samples was enhanced by the use of an electron flood gun. The samples were not sputter-cleaned before measurement. In order to compare all spectra recorded, the C 1 s core level attributed to adventitious carbon present in the samples was used as a reference, whose binding energy was fixed at 284.6 eV. Peaks areas of nickel species including satellites were fitted with a non-linear least squares fitting program using a properly weighted sum of Lorentzian and Gaussian component curves after background subtraction according to Shirley.

In addition to XRD, TEM and BET measurements, and mainly focused on the analysis of the extent of coking, the used catalysts were characterised by Raman spectroscopy and dynamic thermogramivetric analysis (TGA) using a TA Instruments TGA 550 thermobalance under atmospheric pressure. The exit stream was monitorised by mass spectrometry (MS) with a Pfeiffer Prisma apparatus. The experiments followed a 5 °C min^{-1} ramp up to a temperature of 850 °C, which was then maintained for 30 min, under a flow of synthetic air.

2.3. Catalytic performance and stability testing

The analysis of the catalytic performance was carried out in a bench-scale fixed-bed reactor at constant temperature (650 °C). The feedstream consisted of a 10%CH_4/10%CO_2/80%N_2 mixture that was admitted into the reactor with a total flow rate of 1,200 mL min^{-1}, which accounted for a gas hourly space velocity of 90,000 h^{-1} defined as the total volumetric flow to the reactor divided by the volume of bed catalyst (0.8 mL). On each experiment, 0.1 g of reduced aluminate precursor (particle size 0.25–0.30 mm) were mixed with 0.9 g of inert quartz (particle size 0.50–0.80 mm) and loaded into the reactor. Each reaction experiment was carried out for 12 h. Additionally, a long-term stability test of the most efficient catalyst for 200 h was carried out. Feed and effluent streams were analysed online by a microGC (Agilent 490) equipped with a thermal conductivity detector and working with He as the carrier gas. Three columns, Molecular Sieve 5 Å (10 m), PBQ (3 m) and PPQ (10 m), were used in a series/bypass arrangement for the complete separation of H_2, N_2, O_2, CH_4, CO and CO_2. A cold trap at the outlet of the reactor was used to condense out any water from the product gas stream.

On the basis of the molar flows at the inlet and outlet of the reactor, conversion (X_{CH4} and X_{CO2}) and product yields (Y_{CO} and Y_{H2}) were calculated according to the following equations:

$$X_{CH_4} = \frac{F_{CH_4,inlet} - F_{CH_4,outlet}}{F_{CH_4,inlet}} \quad (1)$$

$$X_{CO_2} = \frac{F_{CO_2,inlet} - F_{CO_2,outlet}}{F_{CO_2,inlet}} \quad (2)$$

$$Y_{H_2} = \frac{F_{H_2,outlet}}{2 \cdot F_{CH_4,inlet}} \quad (3)$$

$$Y_{CO} = \frac{F_{CO,outlet}}{F_{CH_4,inlet} + F_{CO_2,inlet}} \quad (4)$$

The thermodynamic data were calculated via the HSC Chemistry software package (Metso Outotec) by the GIBBS solver using the so-

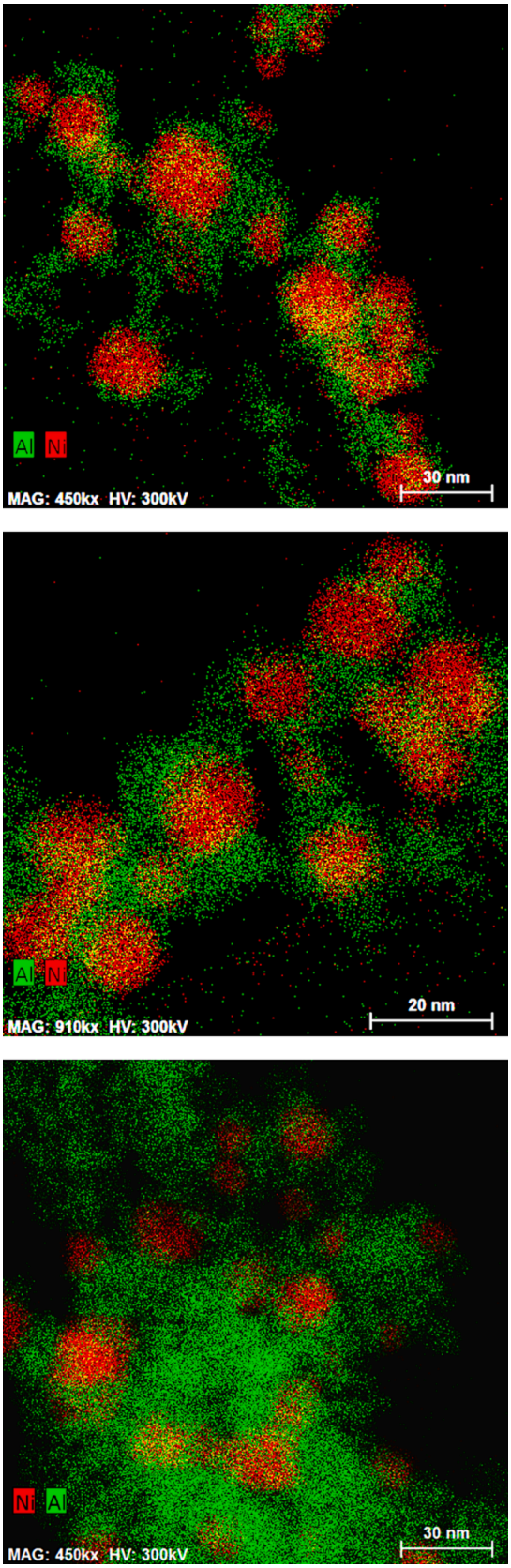

Fig. 5. STEM/EDS elemental maps of the reduced Ni/Al_2O_3 catalysts derived from the stoichiometric (NiAl(33) (figure at the top), sub stoichiometric (NiAl (21) (figure in the middle) and sub-stoichiometric (NiAl(14) (figure at the bottom) $NiAl_2O_4$ precursors.

called Gibbs Energy Minimisation Method. Thus, the program calculates the amounts of products at equilibrium under isothermal and isobaric conditions, when the multi-component equilibrium composition is determined by a number of simultaneous reactions. The only requirement is the specification of the substances and potentially stable phases to be taken into account in the calculations as well as the amounts and temperatures of raw materials, which can easily be made in the HSC program interface. Thus, in addition to solid carbon, the following gaseous substances were considered: CH_4, N_2, CO, CO_2, H_2 and H_2O.

3. Results and discussion

3.1. Physico-chemical characterisation of the $NiAl_2O_4$-based precursors

The elemental composition of the prepared $NiAl_2O_4$-like precursors was determined by WDXRF. The experimental Ni/Al molar ratios of the precursors, summarised in Table 1, were notably similar to the nominal values with maximum deviations lower than 10%. Thus, the corresponding nickel content varied from 5 to 33%wt. The textural properties of the calcined spinels were investigated by N_2 physisorption. The resulting adsorption/desorption isotherms (Figure S1, Supplementary Material) were comparable to those designated as type IV(a), according to the classification given by IUPAC [36]. These were features of mesoporous materials. The hysteresis loops displayed by the isotherms were, in turn, classified as type H2(b), which was associated with pore blocking over a wide pore size distribution. The specific surface area and pore volume of the various oxides are presented in Table 1.

The specific surface area of the oxide precursors revealed an inverse relationship with the Ni/Al molar ratio, varying from 71 $m^2\,g^{-1}$ for the stoichiometric sample (NiAl(33)), to 122 $m^2\,g^{-1}$ for the counterpart with the lowest ratio (NiAl(5)). Simultaneously, the pore volume of the samples followed a comparable trend, being 0.20 $cm^3\,g^{-1}$ for the stoichiometric precursor and growing up to 0.30 $cm^3\,g^{-1}$ for the sample with a Ni/Al molar ratio of 0.05. The pore size distributions (Figure S2, Supplementary Material) revealed a unimodal profile with the maximum centred at around 75 Å, with the exception of the NiAl(33) oxide whose maximum was located at 90 Å. These results evidenced that the co-precipitation route used for the synthesis of the precursors was able to produce samples with significantly good textural properties.

The structural properties of the precursors were investigated by XRD, Raman spectroscopy, HRTEM and STEM/EDS mapping. The X-Ray diffractograms of the samples are shown in Fig. 1. All synthesised precursors exhibited signals located at $2\theta = 19.1$, 31.4, 37.3, 45.1, 59.6 and 65.5°, which were attributed to a $NiAl_2O_4$ spinel-like phase (ICDD 00–10-0339). The crystallite size of the $NiAl_2O_4$ phase, estimated by the Scherrer equation, decreased with the Ni content, from 15 nm for NiAl (33) to 8 nm for NiAl(5). Moreover, the Ni-rich oxides, namely NiAl(21), NiAl(24), NiAl(29) and NiAl(33), presented two additional signals at $2\theta = 43.3$ and 62.9°, thus revealing the presence of segregated NiO (ICDD 00–47-1049) with an average crystallite size of 8 nm. This observation suggested that Ni insertion into the spinelic lattice was not fully achieved [37]. A close-up view of the most intense signal of the spinel phase ($2\theta = 37.3°$), as presented in Figure S3 Supplementary Material, revealed a marked shift towards higher positions (from 37.2 to 37.7°) for decreasing Ni/Al molar ratios, which pointed to a shrinkage of the cell unit of this phase. In this sense, the evolution of the cell parameter of the cubic spinel phase with the Ni/Al molar ratio is shown in Figure S4, Supplementary Material. Hence, the cell parameter decreased from 8.01 Å for the precursors with Ni loadings between 33 and 24%wt. down to 7.93 Å for the precursor with the lowest Ni loading (5%wt.). Note that the cell parameter of the cubic phase of pure γ-Al_2O_3 was 7.91 Å. Thus, these results would suggest that the detected cubic spinel phase resembled more and more to the pure γ-Al_2O_3 with lower Ni/Al molar ratios. Moreover, a deconvolution of the aforementioned spinelic diffraction signal, as shown in Figure S3, Supplementary Material, actually evidenced that this was derived from two contributions centred

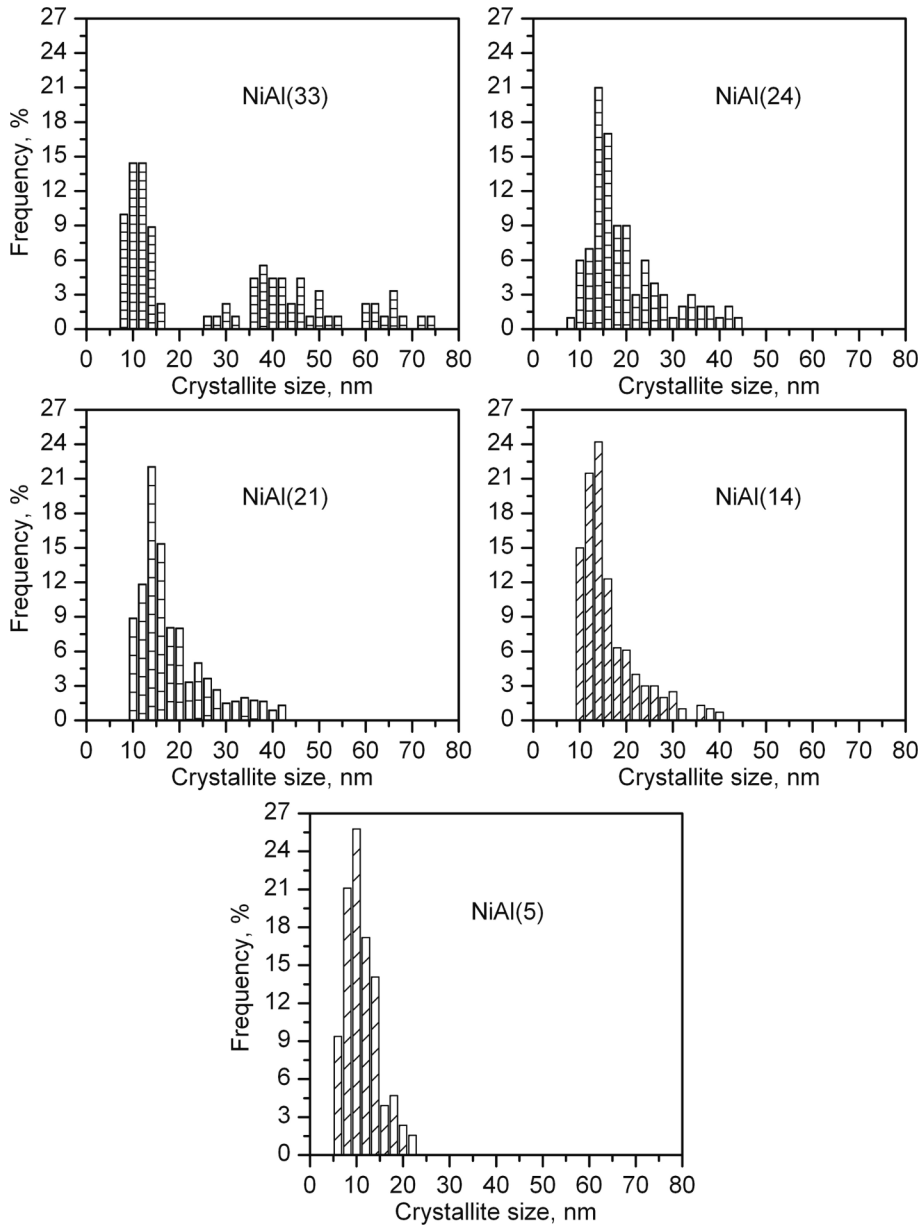

Fig. 6. Ni crystal size distributions of selected reduced Ni/Al_2O_3 catalysts.

at 37.1° ($NiAl_2O_4$) and 37.7° (γ-Al_2O_3). Thus, the shift of the overall cubic phase signal was a consequence of the decrease of intensity of the contribution of $NiAl_2O_4$ phase and the simultaneous increase in intensity of the γ-Al_2O_3 phase unavoidably formed owing to Ni deficiency in the samples with lower Ni/Al molar ratios.

These findings were also confirmed by the Raman spectra of the calcined precursors, as shown in Figure S5, Supplementary Material. Hence, the spectra of all samples exhibited the two bands associated with the presence of the $NiAl_2O_4$ spinel, located at 370 and 570 cm^{-1} [38], in the same position and with similar width, thus evidencing that the $NiAl_2O_4$ present in all of them possessed the same chemical structure. Likewise, several bands attributed to the presence of segregated NiO were observed at 480, 690, 1080 and 1360 cm^{-1} [39], although those were only visible for the precursors with Ni/Al molar ratios higher than 0.25 (NiAl(21), NiAl(24), NiAl(29) and NiAl(33)).

The structure of selected calcined precursors (NiAl(33), NiAl(21) and NiAl(14) samples) was also studied by STEM analysis coupled with EDS mapping (Fig. 2). The maps clearly revealed the presence of Ni clusters, probably attributable to the segregated NiO crystallites with sizes around 10 nm in line with XRD results, in the structure of the NiAl(33) oxide. On the other hand, the composited map of the sub-stoichiometric NiAl(14) and NiAl(21) precursors evidenced a higher dispersion of the Ni atoms and an intimate mixing with the Al species, thus suggesting a better structural homogeneity of these samples. Apparently, while some small Ni clusters were still visible in the NiAl(21) sample, these were not detected for the NiAl(14) counterpart. Moreover, an EDS elemental analysis of these clusters (zone 1 in Figure S6, Supplementary Material) revealed a Ni/O molar ratio of approximately 1, thus confirming that these clusters were composed of NiO. The presence of NiO crystallites was further confirmed with HRTEM micrographs of the NiAl(33) calcined precursor. Indeed, as shown in Figure S6, Supplementary Material, crystals of around 7–10 nm were present. Their FFT analysis revealed the (1 1 1) and (2 0 0) planes of the NiO crystalline structure.

The distribution of nickel species (Ni^{2+} as NiO and Ni^{2+} belonging to a spinel-like lattice) was estimated by H_2-TPR. As revealed by Fig. 3, the reduction profiles of the precursors followed a two-step process according to Equations (5) and (6). Thus, at temperatures between 350 and 650 °C the reduction of segregated NiO to metallic Ni occurred [40].

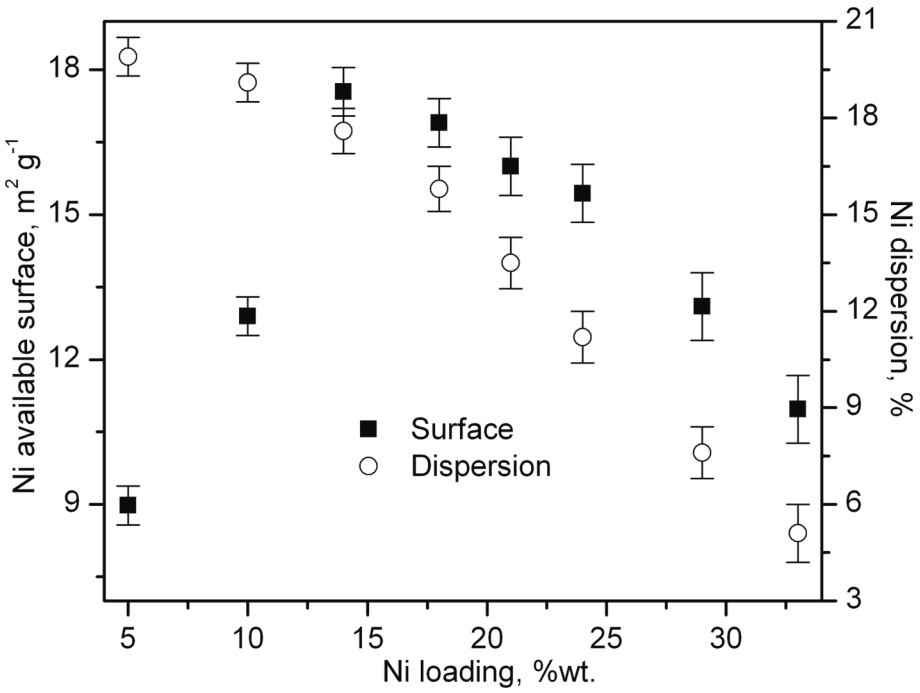

Fig. 7. Evolution of the Ni dispersion and available surface of the reduced Ni/Al_2O_3 catalysts with the Ni loading of the $NiAl_2O_4$ precursors.

Nevertheless, for the precursors with Ni/Al molar ratios lower than 0.20 (namely, NiAl(5), NiAl(10), NiAl(14) and NiAl(18)), the contribution of the low-temperature step was significantly small and virtually negligible for the NiAl(5) precursor. Above 650 °C, the reduction of the aluminate phase to metallic Ni and γ-Al_2O_3 took place [41]. It must be pointed out that this reduction process was usually completed at 950 °C, thus evidencing the notable stability of these Ni-Al mixed oxides.

$$NiO + H_2 \rightarrow Ni + H_2O \quad (5)$$

$$NiAl_2O_4 + H_2 \rightarrow Ni + H_2O + Al_2O_3 \quad (6)$$

The integration and quantification of the TPR traces allowed for the estimation of the overall H_2 consumption and the H_2 uptake associated with each step (50–650 °C and 650–950 °C), as summarised in Table 2. Initially it was verified that the experimental total uptake was in fairly good agreement with the theoretical consumption (17.0 mmol H_2 g_{Ni}^{-1}). Likewise, the relative abundance of Ni^{2+} species as nickel aluminate was estimated according to the following equation:

$$NiAl_2O_4 fraction = \frac{H_2 uptake(NiAl_2O_4)}{H_2 uptake(NiAl_2O_4) + H_2 uptake(NiO)} \cdot 100 \quad (7)$$

It could be clearly inferred that the presence of $NiAl_2O_4$ was gradually favoured for lower nickel loadings. Thus, the samples with 5–18% wt.Ni presented a relative content of the aluminate phase higher than 90%, thereby revealing a good structural homogeneity. On the contrary, a marked segregation of Ni as NiO was noticed over the Ni-rich oxides, up to 30% for the NiAl(33) sample, in line with the previous findings revealed by XRD and STEM-EDS and HRTEM.

When using co-precipitation as synthesis route, the incomplete insertion of the nickel species into the spinel lattice largely depends on several factors including the nature of nickel and aluminium salts, pH, precipitating agent, temperature, and aging of the precipitate among others, and the applied thermal activation to induce the formation of the spinel. The latter, given that the solid-state reactions for the formation of the aluminate spinels tend to present relatively slow kinetics, is probably the most critical step. Thus, under relatively mild calcination conditions (namely 850 °C/4 h, in this study) it is not unlikely that a fraction of nickel remains as NiO. Expectedly, a higher calcination temperature (above 1000–1100 °C) certainly would result in a NiO-free nickel aluminate phase (all Ni^{2+} species will be in the form of $NiAl_2O_4$). Unfortunately, these severe thermal conditions also would produce oxides with a significantly lower surface area and a poorer catalytic performance.

X-ray photoelectron spectroscopy was used to provide information about the oxidation state and the chemical environment of the nickel present on the surface of two selected calcined spinel-type oxides, namely NiAl(33) and NiAl(14). Thus, the Ni2$p_{3/2}$ spectra (850–870 eV) were deconvoluted into five signals (Figure S7, Supplementary Material). The three main signals were centred at around 853.9, 855.4 and 856.9 eV and were associated with the presence of Ni^{2+} (NiO), Ni^{2+} (nickel belonging to a spinelic phase) and Ni^{3+} (Ni_2O_3) species, respectively [42]. The satellite contribution of the spectra was dominated by an intense signal located at 861.0 eV, characteristic of the presence of Ni^{2+}, and a small shoulder at 865.3 eV, which was a consequence of the relatively reduced presence of Ni^{3+} ions in these samples. The Ni2$p_{3/2}$ spectrum of the NiAl(33) oxide clearly evidenced the presence of comparable amounts of nickel oxide and nickel aluminate. Hence, in addition to traces of Ni^{3+} species, the observed nickel was in the form of NiO (34%) and $NiAl_2O_4$ (42%). In the case of the NiAl (14) sample the relative abundance of nickel oxide was substantially lower (8%). In sum, these XPS results corroborated the co-existence of NiO and $NiAl_2O_4$ phases in the stoichiometric aluminate precursor, and the preferential formation of a spinel-type lattice in the examined sub-stoichiometric precursor.

3.2. Physico-chemical characterisation of the reduced Ni/Al_2O_3 catalysts

The N_2 physisorption isotherms of the reduced Ni catalysts (Ni/Al_2O_3) were comparable to those exhibited by the $NiAl_2O_4$ precursors (Figure S8, Supplementary Material), thus showing type IV(a) isotherms with H2(b) hysteresis cycles as well, as expected for nickel catalysts supported on mesoporous γ-Al_2O_3. The specific surface area and pore volume of the catalysts, listed in Table 3, varied between 54 and 96 m^2/g^{-1} and 0.15 and 0.22 $cm^3\ g^{-1}$, following the same trend as for the calcined mixed oxides that pointed out better textural properties for the samples with lower Ni loadings. The appreciable loss of textural

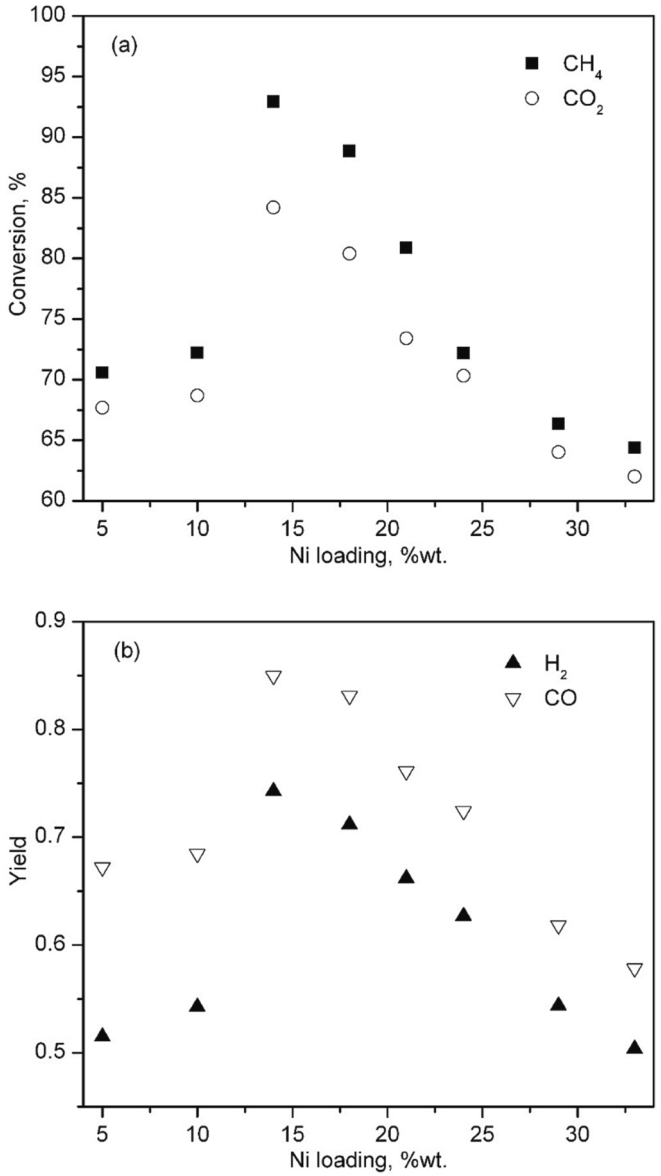

Fig. 8. Evolution of the (a) CH_4 and CO_2 conversions and (b) H_2 and CO yields with the Ni loading of the $NiAl_2O_4$ precursors.

properties was due to the high temperatures employed in the reduction process (850 °C for 2 h) [43].

As for the average pore size (Figure S9, Supplementary Material), this ranged between 98 Å (NiAl(5)) and 108 Å (NiAl(29)). A markedly larger diameter was observed for the NiAl(33) catalyst. In all cases the mean pore size of the reduced catalyst was larger than that of the corresponding calcined spinelic precursor.

The X-Ray patterns of the reduced Ni/Al_2O_3 catalysts (Fig. 4) displayed several signals located at $2\theta = 45.0$, 52.0 and 76.7°, which were attributed to the presence of exsolved metallic Ni (ICDD 00–004-0850). Consistently, the intensity of these signals increased with the Ni/Al molar ratio. No signals associated with any oxidised Ni species were detected, thus validating the selected reduction treatment for the synthesised precursors. Additional diffraction peaks located at 19.4, 32.0, 37.7, 39.7, 45.8 and 66.9°, assigned to a cubic phase of γ-Al_2O_3 (ICDD 01–074-2206), were observed, in agreement with the expected phases of the full reduction of $NiAl_2O_4$-like oxides. The metallic Ni crystallite size (Table 3), estimated by the Scherrer equation from the signal located at $2\theta = 52.0°$, varied between 8 and 15 nm. A progressive enlargement of the metallic crystallites was evident when the nickel content increased.

The FFT of the HRTEM images and the quantification of the elemental maps determined by STEM/EDS of the reduced NiAl(33), NiAl (21) and NiAl(14) oxides provided more insights on the structure of the reduced catalysts. As shown in Fig. 5, the catalyst derived from the stoichiometric precursor presented clearly defined clusters of Ni between 20 and 30 nm in size. On the other hand, the catalysts derived from the sub-stoichiometric precursors exhibited significantly smaller Ni clusters, around 10–20 nm. More precise information on the nickel particle size, dispersion and metallic surface area was obtained from STEM/HAADF micrographs (Figure S10, Supplementary Material). Hence, a particle size distribution was defined by measuring the size of at least 150 crystals for each sample. From these results, an average crystallite size could be calculated, as follows:

$$d = \frac{\sum d_i \cdot n_i}{\sum n_i} \tag{8}$$

where n_i is the number of counted particles with size d_i. The results, included in Fig. 6, evidenced a general decrease in the average Ni crystallite size with the Ni/Al molar ratio, from 29 nm for the stoichiometric spinel to 12 nm for the sample with the lowest Ni/Al molar ratio. Furthermore, for the reduced catalysts resulting from the Ni-rich precursors (with a Ni/Al molar ratio of 0.3, 0.4 and 0.5) the Ni crystals presented two different size distributions: small crystals (around 10 nm) formed from reduction of the $NiAl_2O_4$ phase, and some large crystals (30–70 nm) generated from the reduction of segregated NiO. Conversely, since the presence of nickel oxide was quite limited in the precursors with lower Ni/Al molar ratios (below 0.20), their respective particle size distributions were substantially narrower, and centred on reduced sizes (about 10 nm).

Based on the average Ni particle size of each catalyst, an attempt to calculate the metallic dispersion (D, %) (Equation (9) and the available surface of metallic Ni (S_{Ni}, $m^2\ g^{-1}$) (Equation (10) could be made. For this purpose, the following equations were used:

$$D = n \cdot \left(\frac{d/2}{A_{at}}\right)^2 \frac{S_{BET} \cdot MW_{Ni}}{A_{image} \cdot C_{Ni} \cdot N_A} \cdot 10^{20} \tag{9}$$

$$S_{Ni} = \frac{A_{at} \cdot C_{Ni} \cdot D \cdot N_A}{MW_{Ni}} \cdot 10^{-22} \tag{10}$$

where A_{at} is the atomic surface area of Ni (0.0649 nm^2), S_{BET} is the specific surface area of the reduced catalyst ($m^2\ g^{-1}$), A_{image} was the area of the TEM image chosen for the calculation (9,000–12,000 nm^2), C_{Ni} is the weight percentage of Ni in the catalyst and MW_{Ni} is the molecular weight of Ni. The results, summarised in Fig. 7, pointed out that the metallic dispersion of nickel increased for lower Ni/Al molar ratios, from 5% for NiAl(33), to 20% for NiAl(5). Consequently, the available metallic surface increased from 11 $m^2\ g^{-1}$ for the stoichiometric catalyst and reached a maximum value (18 $m^2\ g^{-1}$) for the catalyst prepared from the precursor oxide with a Ni/Al molar ratio 0.15 (NiAl(14)). It should be pointed out that, although the NiAl(5) catalyst exhibited the largest total surface area (96 $m^2\ g^{-1}$) and the highest nickel dispersion, its estimated Ni surface area, which also depends on the nickel content (5%wt.), was markedly low (9 $m^2\ g^{-1}$).

3.3. Catalytic performance of the reduced Ni/Al_2O_3 catalysts

The performance of the reduced $NiAl_2O_4$-mediated Ni/Al_2O_3 catalysts was studied at constant temperature of 650 °C and 90,000 h^{-1}. The evolution of the reactant conversions (CH_4 and CO_2) and products yields (H_2 and CO) with time (12 h) are shown in Figure S11, Supplementary Material. These kinetic data were obtained operating with a total flowrate of 1,200 mL min^{-1}, which resulted in a linear velocity higher than 30 cm s^{-1}. Under these conditions, effects of external transfer resistances could be neglected. Additionally, it was checked that the pressure drop was lower than 20% of the total operation pressure in the

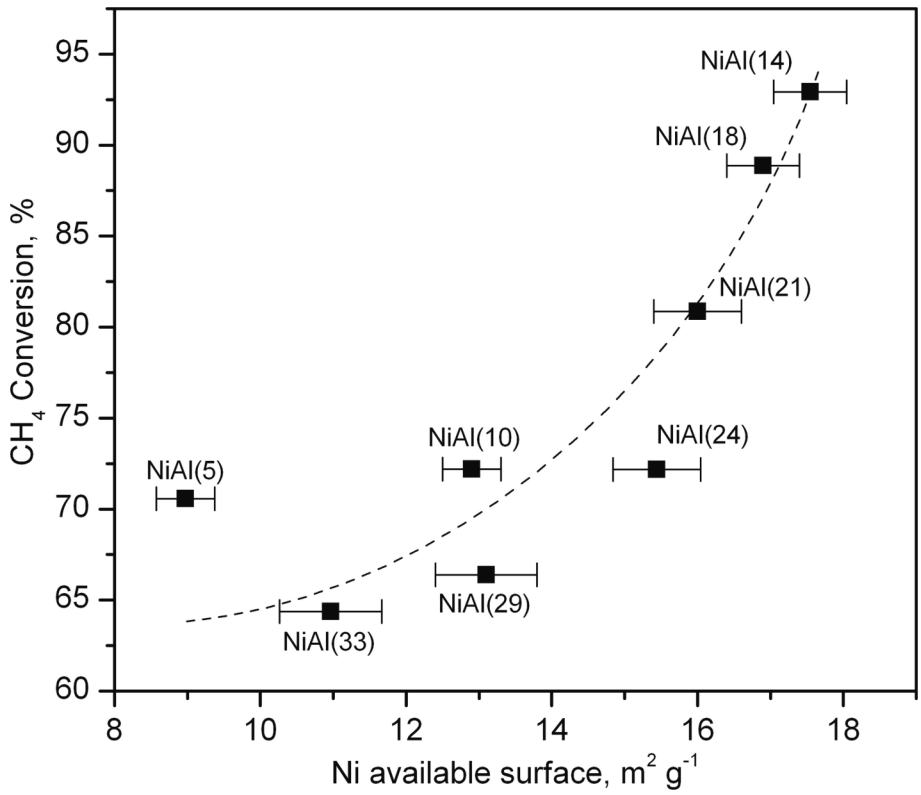

Fig. 9. Relationship between the Ni surface available and the CH_4 conversion of the reduced Ni/Al_2O_3 catalysts.

Table 4
Physico-chemical properties of the Ni/Al_2O_3 catalysts of used catalysts (12 h).

Sample	S_{BET}, m^2/g^{-1}	Ni crystallite size, nm	Coke generation, $g_C\ g_{CAT}^{-1}$
NiAl(5)	93 (96)	7 (8)	< 0.01
NiAl(10)	86 (88)	9 (10)	< 0.01
NiAl(14)	83 (85)	10 (10)	< 0.01
NiAl(18)	78 (78)	11 (11)	0.01
NiAl(21)	70 (70)	12 (12)	0.04
NiAl(24)	70 (68)	12 (12)	0.05
NiAl(29)	61 (57)	13 (12)	0.30
NiAl(33)	59 (54)	14 (15)	0.66

The values in parentheses correspond to the freshly reduced catalysts.

reactor. Finally, the possibility of internal pore diffusional was examined by measuring conversions at fixed conditions (650 °C) for catalysts (NiAl (14)) particles of different size (0.16–0.25, 0.25–0.3, 0.3–0.5 and 0.5–1 mm), and the results showed that pore diffusional resistance was absent for particles less than 0.5 mm in diameter, as evidenced by Figure S12, Supplementary Material. Then, the absence of transfer limitations could be assumed.

Thus, three different behavioural trends could be observed in terms of both activity and stability of the samples. On one hand, the NiAl(14) and NiAl(18) catalysts exhibited the highest CH_4 conversion (88–93%) and a very good stability. Although the NiAl(21) sample also showed an appreciable initial conversion (86%), its performance was not stable since a decay in conversion was observed (81% after 12 h). On the other hand, the two spinel-derived catalysts with the lowest Ni loadings (NiAl (5) and NiAl(10) samples) were considerably less active (68–73%) but

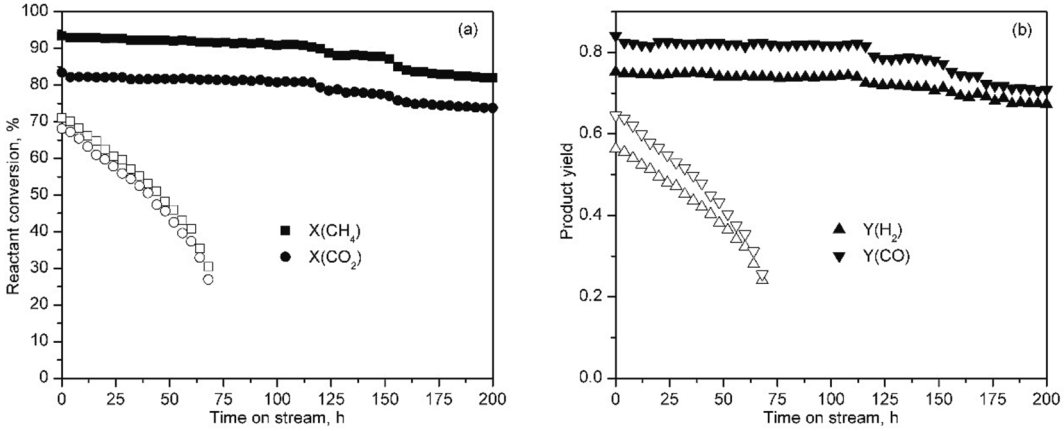

Fig. 10. Evolution of the CH_4 conversion (a), CO_2 conversion (a), H_2 yield (b) and CO yield (b) with time on stream of the reduced Ni/Al_2O_3 catalysts derived from the NiAl(14) (hollow symbols) and NiAl(33) precursors (filled symbols).

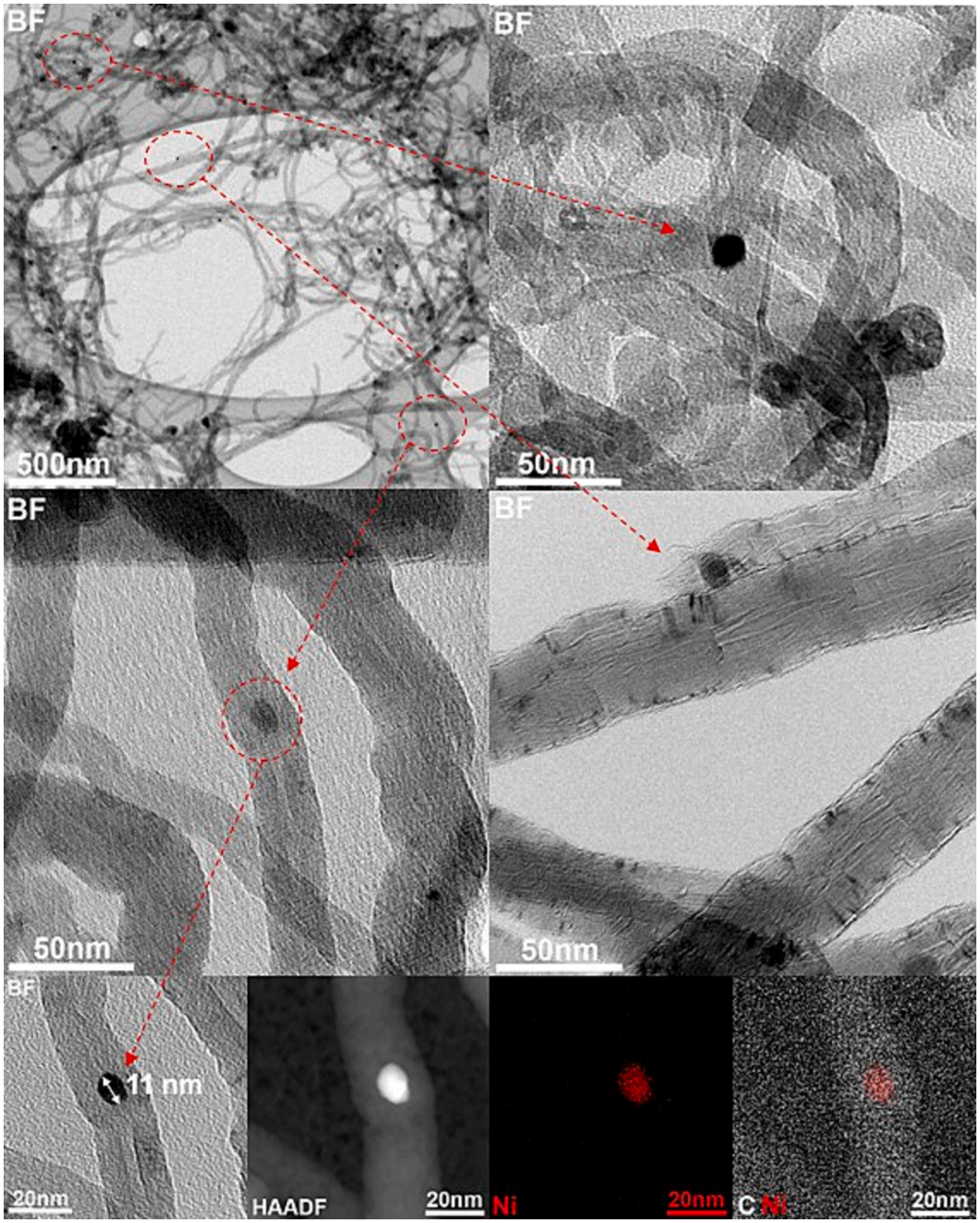

Fig. 11. TEM/HAADF and STEM/EDS micrographs of the carbonaceous deposits on the NiAl(14) catalyst after 200 h of reaction time.

were interestingly quite stable. Finally, the remaining three catalysts, which were the samples with the highest Ni loading, namely NiAl(24), NiAl(29) and NiAl(33), evidenced a reasonable initial activity (71–74%) but their performance with time was poor with a continuous decrease in conversion, particularly relevant for the NiAl(29) and NiAl(33) samples. In this case, and also valid for the NiAl(21) catalyst, deactivation was possibly due to the deposition of coke on the catalyst surface. Recall that coke formation is significantly favoured at lower temperatures, mainly due to Boudouard reaction (Equation (11) being notably exothermic, and methane cracking (Equation (12) being endothermic but with a relatively low reaction enthalpy [44].

$$2CO \leftrightarrow C + CO_2 \quad (11)$$

$$CH_4 \leftrightarrow C + 2H_2 \quad (12)$$

The very same findings were observed regarding the activity and stability as a function of CO_2 conversions and product (H_2 and CO) yields. It must be noticed that CH_4 conversions were higher than CO_2 conversions for all catalysts. This difference was particularly remarkable for the most active catalysts, which was also a consequence of the aforementioned secondary reactions consuming CH_4 (methane cracking) and forming CO_2 (Boudouard reaction) [45,46]. At this point, it should be noted that the RWGS (Equation (13), as a side reaction that consumes CO_2, is not favoured at 650 °C.

$$CO_2 + H_2 \leftrightarrow CO + H_2O \quad (13)$$

Comparing the obtained conversions and yields with the corresponding equilibrium values (Figure S13, Supplementary Material) it was clear that only the NiAl(14) and NiAl(18) catalysts were able to achieve CH_4 conversions near the equilibrium value (93.8%), with H_2

yields also relatively close to the equilibrium yield (0.80). On the other hand, all substoichiometric catalysts achieved CO_2 conversions significantly higher than the calculated equilibrium value (65.3%) with CO yields also surpassing the equilibrium yield (0.52). These results pointed out that the nickel catalysts, especially those samples with higher Ni dispersions, were not very active in the reverse water gas shift [47]. Thus, H_2/CO molar ratios around 0.85 were obtained.

On the other hand, the dependence of these kinetic parameters on the Ni loading of the precursors (Fig. 8) evidenced an optimal value for the CH_4 and CO_2 conversions for a Ni/Al = 0.15, which was equivalent to a 14%wt.Ni loading. This highly efficient performance for NiAl(14) was also observed for both H_2 and CO yields vs. the Ni content. As suggested by Fig. 9, these results were well correlated with the available Ni surface, thus evidencing that this catalytic property was the parameter that controlled the behaviour of the $NiAl_2O_4$-mediated catalysts.

The performance of this optimal catalyst was generally superior to that of other comparable catalysts found in the literature. For instance, Qiu et al. [48] and Tillmann et al. [49] achieved CH_4 conversions of around 75% with a 15%wt.Ni/Al_2O_3 catalyst, although the former did it 700 °C and 7,200 mL CH_4 g_{cat}^{-1} h^{-1} and the latter did it at 820 °C and 206,000 mL CH_4 g_{cat}^{-1} h^{-1}. It must be noticed that most of the research studies in this topic carry out the reaction tests at relatively low space velocities. For example, Dang et al. [50] prepared an optimal catalyst with a 10%wt. loading of Ni that achieved around 80% CH_4 conversion at 700 °C and 6,000 mL CH_4 g_{cat}^{-1} h^{-1}, while Zhang et al. [51] achieved over 95% CH_4 conversion at 800 °C and 11,250 mL CH_4 g_{cat}^{-1} h^{-1} with a series of Ni catalysts supported over mesoporous silica with Ni loadings varying from 2.5 to 15%wt. In addition to that, other studies have focused on even lower Ni loadings. Such is the case of Bian et al. [52], which attained CH_4 conversions over 90% at 750 °C with a 5%wt.Ni/Al_2O_3 at 30,000 mL CH_4 g_{cat}^{-1} h^{-1}, and Moradi et al. [53], which studied a 5%wt.Ni/ZSM-5 catalyst that obtained 90% CH_4 at 700 °C and 6,000 mL CH_4 g_{cat}^{-1} h^{-1}. Given the low temperature (650 °C) and high space velocity (72,000 mL CH_4 g_{cat}^{-1} h^{-1}) employed in our research work, the NiAl(5) catalyst can also be deemed to be more active than these two catalysts, despite achieving a lower CH_4 conversion.

The used catalysts were characterised by N_2 physisorption, XRD, Raman spectroscopy and thermogrametric analysis (TGA) in order to determine possible effects of the reaction environment on their physicochemical properties of the catalysts and to examine the extent of coke formation. The XRD patterns of the spent catalysts, shown in Figure S14, Supplementary Material, only revealed the presence of metallic Ni and γ-Al_2O_3, thus ruling out the possibility of a bulk reoxidation of the catalysts during the reaction. Furthermore, the characteristic signal of graphitic carbon at 2θ = 26.7° was clearly observed for the catalysts with higher Ni/Al molar ratios (NiAl(33) and NiAl(29)) and, although less noticeably, for the NiAl(24) and NiAl(21) samples as well [54]. The quantification of the extent of coking was carried out by thermogravimetry coupled to mass spectrometry. The corresponding thermograms (Figure S15, Supplementary Material) presented three distinct mass-change steps: a first mass loss from ambient temperature up to 200 °C associated with the desorption of water followed by a mass gain between 250 and 450 °C due to oxidation of the Ni crystallites, and finally a second mass loss attributed to coke combustion at temperatures over 500 °C and peak combustion temperatures at around 620 °C. This last mass change, assigned to the combustion of graphitic carbon [55], was only clearly observed for the Ni-rich samples (NiAl(24), NiAl(29) and NiAl(33)). The integration and quantification of this combustion step allowed to calculate the amount of coke present in these samples, as shown in Table 4. It must be pointed out that the negligible presence of CO_2 in the outflow stream at low temperatures ruled out the occurrence of coke combustion during the oxidation of the metallic nickel in the 250–450 °C range (Figure S15, Supplementary Material).

The results evidenced that coke deposition was almost negligible (lower than 0.01 g_C g_{CAT}^{-1}) for all catalysts with a Ni loading lower than 18%wt., which demonstrated the high coking resistance of the Ni catalysts derived from these substoichiometric spinels with a Ni particle size bellow 15 nm. This contrasts with the noticeable coke formation over the Ni-rich samples (up to 0.66 g_C g_{CAT}^{-1} for the NiAl(33) catalyst). This finding was related to the higher propensity for coking shown by the Ni particles with a large size (25–75 nm), which were rather abundant (50–60% of the particles) over the NiAl(29) and NiAl(33) samples. The characterisation by Raman spectroscopy of the used Ni/Al_2O_3 catalysts (Figure S16, Supplementary Material) revealed the presence of two bands in the 1100–1800 cm^{-1} range: the so-called D band located at 1360 cm^{-1} and associated with carbon with structural imperfections, and the so-called G-band, centred at 1580 cm^{-1}, attributed to the presence of layered graphite [56,57].

In line with the thermogravimetric results, the intensity of these two bands largely depended on the Ni loading, with the catalysts prepared with the highest Ni/Al ratios (0.50 and 0.40) exhibiting notably intense bands. For decreasing values of the Ni/Al molar ratio these signals were less noticeable. The notable coke formation over the Ni-rich catalysts was responsible for the marked decay in the reactant conversions and product yields underwent by the NiAl(33) and NiAl(29) catalysts. Judging from the relative intensity of G and D bands, a favoured formation of graphitic carbon was expected. It is worth pointing out that although the extent of coke formation over the Ni-deficient catalysts (Ni/Al < 0.2) was very low, the presence of traces of carbonaceous nanotubes could be detected, as revealed by the TEM micrographs of the used NiAl(14) sample (Figure S17, Supplementary Material). On the other hand, the average size of the Ni crystallites, estimated by the Scherrer equation and included in Table 4, did not evidence appreciable sintering on the catalysts as they were comparable to those exhibited by the freshly reduced samples. In line with these results, the specific surface areas of the used catalysts (Table 4), measured by N_2 physisorption, did not vary significantly.

Finally, long-term stability tests with the most active catalyst (NiAl(14) sample) and the stoichiometric counterpart (NiAl(33) sample), for reference, were carried out by subjecting them to a reaction run for a period of 200 h (650 °C, 90,000 h^{-1}). The evolution of the reactant conversions and product yields with time on stream, depicted in Fig. 10, evidenced that the optimal substoichiometric catalyst was able to operate stably for around 120 h, during which the CH_4 and CO_2 conversion levels only slightly decreased from 93%/83% to 90%/80%, respectively. After the 120-hour mark, a marked decrease in conversion was observed (from 90%/80% to 87%/77%), after which the catalyst continued to operate in a stable way for additional 30 h. Finally, after 150 h of operation, the conversion levels again decreased down to 84%/75%. After 200 h conversion was 81%/73%. On the other hand, the reference stoichiometric catalyst could not operate for the whole duration of the experiment due to a dramatic deactivation. Hence, conversion levels continuously decreased from 71%/67% at the start of the experiment down to 30/26% after only 70 h of reaction time. The experiment was stopped to avoid the plugging of the reactor. On the other hand, the product yields showed similar trends, although it was noticed that the H_2 yield decreased slightly more with time on stream than the CO yield for both catalysts. Hence, the H_2/CO molar ratio of the product streams varied between 0.85 and 0.80 for the whole duration of the experiment.

After the stability tests, direct gravimetric measurements indicated that the amount of generated coke over the NiAl(14) catalyst after extended time on stream (200 h) was 1 g_C g_{CAT}^{-1}. Accordingly, the XRD pattern of the catalyst after this reaction run (Figure S18, Supplementary Material) revealed a very intense diffraction signal at 2θ = 26.7°, which was not observable on the fresh catalyst nor after 12 h of reaction time, indicative of the aforementioned massive coke deposition. Additionally, the Ni crystallite size estimated from this XRD pattern was 11 nm, thus ruling out sintering of the metallic nickel during the reaction. Note that this size (11 nm) was quite similar, within the experimental error, to 10 nm observed for the freshly reduced counterpart. These results were confirmed by TEM/HAADF micrographs of the used catalyst. Hence, as

shown in Fig. 11, a significant amount of carbonaceous deposits, mainly in the form of nanotubes, were formed. Moreover, the Ni crystallites that were observed embedded in these nanotubes maintained an average size of 10–15 nm, in line with the estimation given by XRD.

It is noteworthy that, despite the massive coke generation, the catalyst still maintained a significant activity after the 200-hour time interval, demonstrating the remarkable stability of the optimised Ni/Al_2O_3 catalyst. On the other hand, the reference NiAl(33) catalyst produced around 1.2 g_C g_{CAT}^{-1} of coke over only 70 h of reaction time. When linearly extrapolated to the total duration of the stability run this would imply the formation of more than three times the amount of coke with respect to the substoichiometric counterpart. Apparently, these results concerning the formation of coke could be associated with the Ni crystallite size of the catalysts (10–15 nm), as it is usually assumed that coke deposition is less favoured for smaller crystallites (ideally < 5 nm) [15].

4. Conclusions

This work focused on the optimisation of the Ni/Al molar ratio of some $NiAl_2O_4$ catalytic precursors from which active Ni/Al_2O_3 catalysts were obtained for the dry reforming of methane reaction. For this purpose, several aluminate precursors, with Ni/Al molar ratios in the substoichiometric range (0.5–0.05) were synthesised by a co-precipitation route. The physico-chemical characterisation of the synthesised precursors indicated that the lower Ni/Al molar ratios favoured the textural and structural properties of the aluminates, with higher specific surface areas and pore volumes and smaller crystallite sizes. The investigation by STEM-HAADF/EDS and H_2-TPR indicated that the formation of the $NiAl_2O_4$ spinel was favoured for lower Ni/Al molar ratios, and thus, the amount of nickel present as segregated NiO significantly decreased. After a suitable high-temperature (850 °C) reduction with H_2, the spinel precursors were transformed into Ni/Al_2O_3 catalysts. The analysis of the Ni crystallite size distributions of the reduced catalysts pointed out that the reduction of the segregated NiO species resulted in large Ni crystallites (30–80 nm), while the reduction of the $NiAl_2O_4$ phase produced crystallites of appreciably smaller sizes (8–20 nm). Thus, it was evidenced that the average Ni crystallite size of the catalysts decreased with the Ni/Al molar ratio, while the Ni dispersion simultaneously increased.

The activity of the reduced catalysts for the DRM reaction (operated at 650 °C and 90,000 h^{-1}) was higher for the substoichiometric catalysts with respect to the stoichiometric counterpart. The performance of $NiAl_2O_4$-mediated catalysts was controlled by the available nickel surface area. Among the studied catalysts, the sample with Ni/Al = 0.15 exhibited the best behaviour, with CH_4 conversions and H_2 yield quite close to the equilibrium values. The highly dispersed Ni catalysts also presented a moderate activity for the RWGS reaction resulting in H_2/CO molar ratios around 0.85. The aforementioned optimal catalyst also exhibited a notable stability, being able to operate continuously for 200 h with only a slight decrease in CH_4 conversion (from 93% to 81%), despite the appreciable formation of carbon nanotubes.

CRediT authorship contribution statement

Andoni Choya: Investigation, Writing - Original Draft. **Beatriz de Rivas:** Methodology, Validation. **Maria Luisa No:** Methodology, Formal analysis. **Jose Ignacio Gutiérrez-Ortiz:** Methodology, Formal analysis. **Ruben López-Fonseca:** Conceptualization, Writing-Reviewing and Editing, Supervision.

Declaration of Competing Interest

The authors declare that they have no known competing financial interests or personal relationships that could have appeared to influence the work reported in this paper.

Data availability

Data will be made available on request.

Acknowledgements

This research was funded by the Spanish Ministry of Science and Innovation (PDC2022-133897-I00 and PID2022-141583OB-I00), Basque Government (IT1509-22) and the University of The Basque Country UPV/EHU (DOCREC21/23). The authors wish to thank the technical and human support provided by SGIker (UPV/EHU). In addition, this work made use of the FEI-TITAN at the SGIker facilities from the UPV/EHU.

Appendix A. Supplementary material

Supplementary data to this article can be found online at https://doi.org/10.1016/j.fuel.2023.130166.

References

[1] Guo Y, Luo L, Liu T, Hao L, Li Y, Liu P, et al. A review of low-carbon technologies and projects for the global cement industry. J Environ Sci 2024;136:682–97. https://doi.org/10.1016/j.jes.2023.01.021.
[2] Gowd SC, Ganeshan P, Vigneswaran VS, Hossain MS, Kumar D, Rajendran K, et al. Economic perspectives and policy insights on carbon capture, storage, and utilization for sustainable development. Sci Total Environ 2023;883:163656. https://doi.org/10.1016/j.scitotenv.2023.163656.
[3] Alaedini AH, Tourani HK, Saidi M. A review of waste-to-hydrogen conversion technologies for solid oxide fuel cell (SOFC) applications: Aspect of gasification process and catalyst development. J Environ Manage 2023;329:117077. https://doi.org/10.1016/j.jenvman.2022.117077.
[4] Sternberg A, Jens CM, Bardow A. Life cycle assessment of CO_2-based C1-chemicals. Green Chem 2017;19:2244–59. https://doi.org/10.1039/c6gc02852g.
[5] Saeidi S, Sápi A, Khoja AH, Najari S, Ayesha M, Kónya Z, et al. Evolution paths from gray to turquoise hydrogen via catalytic steam methane reforming: Current challenges and future developments. Renew Sust Energ Rev 2023;183:113392. https://doi.org/10.1016/j.rser.2023.113392.
[6] Ingale GU, Kwon H, Jeong S, Park D, Kim W, Bang B, et al. Assessment of greenhouse gas emissions from hydrogen production processes: turquoise hydrogen vs. steam methane reforming 2022:15. https://doi.org/10.3390/en15228679.
[7] Zhu L, Li L, Fan J. A modified process for overcoming the drawbacks of conventional steam methane reforming for hydrogen production: Thermodynamic investigation. Chem Eng Res Design 2015;104:792–806. https://doi.org/10.1016/j.cherd.2015.10.022.
[8] Hermesmann M, Müller TE. Green, turquoise, blue, or grey? Environmentally friendly hydrogen production in transforming energy systems. Prog Energ Combust 2022;90:100996. https://doi.org/10.1016/j.pecs.2022.100996.
[9] Ning H, Li Y, Zhang C. Recent progress in the integration of CO_2 capture and utilization 2023;28. 10.3390/molecules28114500.
[10] Kumar R, Kumar A, Pal A. Overview of hydrogen production from biogas reforming: Technological advancement. Int J Hydrogen Energy 2022;47:34831–55. https://doi.org/10.1016/j.ijhydene.2022.08.059.
[11] Xu D, Li W, Ge Q, Xu H. A novel process for converting coalmine-drained methane gas to syngas over nickel–magnesia solid solution catalysts. Fuel Process Technol 2005;86:995–1006. https://doi.org/10.1016/j.fuproc.2004.11.014.
[12] Wang Y, Yao L, Wang S, Mao D, Hu C. Low-temperature catalytic CO_2 dry reforming of methane on Ni-based catalysts: A review. Fuel Process Technol 2018;169:199–206. https://doi.org/10.1016/j.fuproc.2017.10.007.
[13] Arora S, Prasad R. An overview on dry reforming of methane: Strategies to reduce carbonaceous deactivation of catalysts. RSC Adv 2016;6:108668–88. https://doi.org/10.1039/c6ra20450c.
[14] Li M, Sun Z, Hu YH. Catalysts for CO_2 reforming of CH_4: a review. J Mater Chem A 2021;9:12495–520. https://doi.org/10.1039/D1TA00440A.
[15] Aramouni NAK, Touma JG, Tarboush BA, Zeaiter J, Ahmad MN. Catalyst design for dry reforming of methane: Analysis review. Renew Sust Energ Rev 2018;82:2570–85. https://doi.org/10.1016/j.rser.2017.09.076.
[16] Alhassan M, Jalil AA, Bahari MB, Owgi AHK, Nabgan W, Hassan NS, et al. Profitable Fischer Tropsch realization via CO_2–CH_4 reforming; an overview of nickel–promoter–support interactions. RSC Adv 2023;13:1711–26. https://doi.org/10.1039/D2RA06773K.
[17] Alipour Z, Babu Borugadda V, Wang H, Dalai AK. Syngas production through dry reforming: A review on catalysts and their materials, preparation methods and reactor type. Chem Eng J 2023;452:139416. https://doi.org/10.1016/j.cej.2022.139416.
[18] Ghanbarabadi H, Khoshandam B. Dry reforming of methane over γ-Al_2O_3 supported NiCo and NiCoCu nano-catalysts. Int J Environ Anal Chem 2023;103:591–611. https://doi.org/10.1080/03067319.2020.1862812.
[19] Chein R, Lu C, Chen W. Syngas production via chemical looping reforming using methane-based feed and NiO/Al_2O_3 oxygen carrier 2022;250:123815. https://doi.org/10.1016/j.energy.2022.123815.

[20] Muraza O, Galadima A. A review on coke management during dry reforming of methane. Int J Energy Res 2015;39:1196–216. https://doi.org/10.1002/er.3295.

[21] Li M, Fang S, Hu YH. Self-stabilization of Ni/Al_2O_3 catalyst with a $NiAl_2O_4$ isolation layer in dry reforming of methane. Catal Lett 2022;152:2852–9. https://doi.org/10.1007/s10562-021-03867-3.

[22] Jiménez-González C, Gil-Calvo M, de Rivas B, González-Velasco JR, Gutiérrez-Ortiz JI, López-Fonseca R. Oxidative steam reforming and steam reforming of methane, isooctane, and N-tetradecane over an alumina supported spinel-derived nickel catalyst. Ind Eng Chem Res 2016;55:3920–9. https://doi.org/10.1021/acs.iecr.6b00461.

[23] Ali S, Gamal A, Khader MM. Development of highly active and coke-resilient Ni-based catalysts for low-temperature steam reformation of methane. Catal Commun 2023;175:106605. https://doi.org/10.1016/j.catcom.2023.106605.

[24] Boukha Z, Jiménez-González C, de Rivas B, González-Velasco JR, Gutiérrez-Ortiz JI, López-Fonseca R. Synthesis, characterisation and performance evaluation of spinel-derived Ni/Al_2O_3 catalysts for various methane reforming reactions. Appl Catal B Environ 2014;158–159:190–201. https://doi.org/10.1016/j.apcatb.2014.04.014.

[25] Fang X, Zhang R, Wang Y, Yang M, Guo Y, Wang M, et al. Plasma assisted preparation of highly active $NiAl_2O_4$ catalysts for propane steam reforming. Int J Hydrogen Energy 2021;46:24931–41. https://doi.org/10.1016/j.ijhydene.2021.05.050.

[26] Gayubo AG, Valecillos J, Iglesias-Vázquez S, Landa L, Remiro A, Bilbao J. Insights into the reaction routes for H_2 formation in the ethanol steam reforming on a catalyst derived from $NiAl_2O_4$ spinel. Energ Fuel 2021;35:17197–211. https://doi.org/10.1021/acs.energyfuels.1c01670.

[27] Claude V, Mahy JG, Geens J, Lambert SD. Ni-doped γ-Al_2O_3 as secondary catalyst for bio-syngas purification: influence of Ni loading, catalyst preparation, and gas composition on catalytic activity. Mater Today Chem 2019;13:98–109. https://doi.org/10.1016/j.mtchem.2019.05.002.

[28] Jiménez-González C, Boukha Z, de Rivas B, González-Velasco JR, Gutiérrez-Ortiz JI, López-Fonseca R. Behaviour of nickel–alumina spinel ($NiAl_2O_4$) catalysts for isooctane steam reforming. Int J Hydrogen Energy 2015;40:5281–8. https://doi.org/10.1016/j.ijhydene.2015.01.064.

[29] García-Gómez N, Valecillos J, Remiro A, Valle B, Bilbao J, Gayubo AG. Effect of reaction conditions on the deactivation by coke of a $NiAl_2O_4$ spinel derived catalyst in the steam reforming of bio-oil. Appl Catal B Environ 2021;297:120445. https://doi.org/10.1016/j.apcatb.2021.120445.

[30] Morales-Marín A, Ayastuy JL, Iriarte-Velasco U, Gutiérrez-Ortiz MA. Nickel aluminate spinel-derived catalysts for the aqueous phase reforming of glycerol: Effect of reduction temperature. Appl Catal B Environ 2019;244:931–45. https://doi.org/10.1016/j.apcatb.2018.12.020.

[31] Kwon Y, Eichler JE, Mullins CB. $NiAl_2O_4$ as a beneficial precursor for Ni/Al_2O_3 catalysts for the dry reforming of methane. J CO_2 Util 2022;63:102112. 10.1016/j.jcou.2022.102112.

[32] Benrabaa R, Barama A, Boukhlouf H, Guerrero-Caballero J, Rubbens A, Bordes-Richard E, et al. Physico-chemical properties and syngas production via dry reforming of methane over $NiAl_2O_4$ catalyst. Int J Hydrogen Energy 2017;42:12989–96. https://doi.org/10.1016/j.ijhydene.2017.04.030.

[33] Zhang S, Yang T, Yu J, Zhan W, Wang L, Guo Y, et al. Robust nanosheet-assembled Al_2O_3-supported Ni catalysts for the dry reforming of methane: the effect of nickel content on the catalytic performance and carbon formation. New J Chem 2021;45:21750–62. https://doi.org/10.1039/D1NJ03954G.

[34] Shamskar FR, Rezaei M, Meshkani F. The influence of Ni loading on the activity and coke formation of ultrasound-assisted co-precipitated $Ni–Al_2O_3$ nanocatalyst in dry reforming of methane. Int J Hydrogen Energy 2017;42:4155–64. https://doi.org/10.1016/j.ijhydene.2016.11.067.

[35] Gil-Calvo M, Jiménez-González C, De Rivas B, Gutiérrez-Ortiz JI, López-Fonseca R. Hydrogen production by reforming of methane over $NiAl_2O_4/Ce_xZr_{1-x}O_2$ catalysts. Chem Eng Trans 2017;57:901–6. https://doi.org/10.3303/CET1757151.

[36] Thommes M, Kaneko K, Neimark AV, Olivier JP, Rodriguez-Reinoso F, Rouquerol J, et al. Physisorption of gases, with special reference to the evaluation of surface area and pore size distribution (IUPAC Technical Report). Pure Appl Chem 2015;87:1051–69. https://doi.org/10.1515/pac-2014-1117.

[37] Nesterov NS, Pakharukova VP, Philippov AA, Gerasimov EY, Tsybulya SV, Martyanov ON. Synthesis of catalytic precursors based on mixed Ni-Al oxides by supercritical antisolvent co-precipitation 2022;12. 10.3390/catal12121597.

[38] Chan Y, Wu C, Shen P, Chen S. Nickel aluminate oxides/hydroxides by pulsed laser ablation of $NiAl_2O_4$ powder in water. Appl Phys A2014;116:1065-73. 10.1007/s00339-013-8183-4.

[39] Mironova-Ulmane N, Kuzmin A, Sildos I, Puust L, Grabis J. Magnon and phonon excitations in nanosized NiO. Latv J Phys Tech Sci 2019;56:61–72. https://doi.org/10.2478/lpts-2019-0014.

[40] Omarov SO, Martinson KD, Matveyeva AN, Chebanenko MI, Nevedomskiy VN, Popkov VI. Renewable hydrogen production via glycerol steam reforming over Ni/CeO2 catalysts obtained by solution combustion method: The effect of Ni loading. Fuel Process Technol 2022;236:107429. https://doi.org/10.1016/j.fuproc.2022.107429.

[41] Bae Y, Hong J. Enhancement of surface morphology and catalytic kinetics of $NiAl_2O_4$ spinel-derived Ni catalyst to promote dry reforming of methane at low temperature for the direct application to a solid oxide fuel cell. Chem Eng J 2022;446:136978. https://doi.org/10.1016/j.cej.2022.136978.

[42] Wan Y, Chen J, Zhan J, Ma Y. Facile synthesis of mesoporous $NiCo_2O_4$ fibers with enhanced photocatalytic performance for the degradation of methyl red under visible light irradiation. J Environ Chem Eng 2018;6:6079–87. https://doi.org/10.1016/j.jece.2018.09.023.

[43] Blas L, Dorge S, Michelin L, Dutournié P, Lambert A, Chiche D, et al. Influence of the regeneration conditions on the performances and the microstructure modifications of $NiO/NiAl_2O_4$ for chemical looping combustion 2015;153:284–93. https://doi.org/10.1016/j.fuel.2015.03.015.

[44] Nikoo MK, Amin NAS. Thermodynamic analysis of carbon dioxide reforming of methane in view of solid carbon formation. Fuel Process Technol 2011;92:678–91. https://doi.org/10.1016/j.fuproc.2010.11.027.

[45] Bao Z, Lu Y, Han J, Li Y, Yu F. Highly active and stable Ni-based bimodal pore catalyst for dry reforming of methane. Appl Catal A 2015;491:116–26. https://doi.org/10.1016/j.apcata.2014.12.005.

[46] Sidik SM, Jalil AA, Triwahyono S, Abdullah TAT, Ripin A. CO_2 reforming of CH_4 over Ni/mesostructured silica nanoparticles (Ni/MSN). RSC Adv 2015;5:37405–14. https://doi.org/10.1039/c5ra04320d.

[47] Rutherford B, Panaritis C, Pahija E, Couillard M, Patarachao B, Shadbahr J, et al. Ni nanoparticles on Co_3O_4 catalyze the reverse water–gas shift with 95% CO selectivity at 300 °C 2023;348:128523. 10.1016/j.fuel.2023.128523.

[48] Qiu H, Ran J, Huang X, Ou Z, Niu J. Unrevealing the influence that preparation and reaction parameters have on Ni/Al_2O_3 catalysts for dry reforming of methane. Int J Hydrogen Energy 2022;47:34066–74. https://doi.org/10.1016/j.ijhydene.2022.08.014.

[49] Tillmann L, Schulwitz J, van Veen A, Muhler M. Dry Reforming of Methane at High Pressure in a Fixed-Bed Reactor with Axial Temperature Profile Determination. Catal Lett 2018;148:2256–62. https://doi.org/10.1007/s10562-018-2453-x.

[50] Dang C, Xia H, Luo J, Cai W. Dendritic layered Ni/Al_2O_3 derived from $NiAl_2O_4$ as high-performance catalyst for dry reforming of methane. Fuel Process Technol 2023;241:107615. https://doi.org/10.1016/j.fuproc.2022.107615.

[51] Wang M, Zhang Q, Zhang T, Wang Y, Wang J, Long K, et al. Facile one-pot synthesis of highly dispersed Ni nanoparticles embedded in HMS for dry reforming of methane. Chem Eng J 2017;313:1370–81. https://doi.org/10.1016/j.cej.2016.11.055.

[52] Bian Z, Zhong W, Yu Y, Wang Z, Jiang B, Kawi S. Dry reforming of methane on Ni/mesoporous-Al_2O_3 catalysts: Effect of calcination temperature. Int J Hydrogen Energy 2021;46:31041–53. https://doi.org/10.1016/j.ijhydene.2020.12.064.

[53] Moradi G, Khezeli F, Hemmati H. Syngas production with dry reforming of methane over Ni/ZSM-5 catalysts. J Nat Gas Sci Eng 2016;33:657–65. https://doi.org/10.1016/j.jngse.2016.06.004.

[54] Owgi AHK, Jalil AA, Aziz MAA, Nabgan W, Hassan NS, Hussain I, et al. The preferable Ni quantity to boost the performance of FSA for dry reforming of methane 2023;332:126124. https://doi.org/10.1016/j.fuel.2022.126124.

[55] Ochoa A, Aramburu B, Valle B, Resasco DE, Bilbao J, Gayubo AG, et al. Role of oxygenates and effect of operating conditions in the deactivation of a Ni supported catalyst during the steam reforming of bio-oil. Green Chem 2017;19:4315–33. https://doi.org/10.1039/C7GC01432E.

[56] Passos AR, Pulcinelli SH, Santilli CV, Briois V. Operando monitoring of metal sites and coke evolution during non-oxidative and oxidative ethanol steam reforming over Ni and NiCu ex-hydrotalcite catalysts. Catal Today 2019;336:122–30. https://doi.org/10.1016/j.cattod.2018.12.054.

[57] Zhang Z, Hu X, Zhang L, Yang Y, Li Q, Fan H, et al. Steam reforming of guaiacol over Ni/Al_2O_3 and Ni/SBA-15: Impacts of support on catalytic behaviors of nickel and properties of coke. Fuel Process Technol 2019;191:138–51. https://doi.org/10.1016/j.fuproc.2019.04.001.